

Strong electron–phonon coupling in magic-angle twisted bilayer graphene

<https://doi.org/10.1038/s41586-024-08227-w>

Received: 24 March 2023

Accepted: 16 October 2024

Published online: 11 December 2024

Open access

 Check for updates

Cheng Chen^{1,2,19}, Kevin P. Nuckolls^{3,4,17,19}, Shuhan Ding⁵, Wangqian Miao⁶, Dillon Wong^{3,4}, Myungchul Oh^{3,4,18}, Ryan L. Lee^{3,4}, Shanmei He², Cheng Peng², Ding Pei¹, Yiwei Li⁷, Chenyue Hao⁸, Haoran Yan⁵, Hanbo Xiao¹, Han Gao¹, Qiao Li¹, Shihao Zhang¹, Jianpeng Liu¹, Lin He⁸, Kenji Watanabe⁹, Takashi Taniguchi¹⁰, Chris Jozwiak¹¹, Aaron Bostwick¹¹, Eli Rotenberg¹¹, Chu Li¹², Xu Han¹², Ding Pan¹², Zhongkai Liu¹, Xi Dai¹², Chaoxing Liu¹³, B. Andrei Bernevig^{4,14,15}, Yao Wang^{5,16}, Ali Yazdani^{3,4} & Yulin Chen^{1,2}

The unusual properties of superconductivity in magic-angle twisted bilayer graphene (MATBG) have sparked considerable research interest^{1–13}. However, despite the dedication of intensive experimental efforts and the proposal of several possible pairing mechanisms^{14–24}, the origin of its superconductivity remains elusive. Here, by utilizing angle-resolved photoemission spectroscopy with micrometre spatial resolution, we reveal flat-band replicas in superconducting MATBG, where MATBG is unaligned with its hexagonal boron nitride substrate¹¹. These replicas show uniform energy spacing, approximately 150 ± 15 meV apart, indicative of strong electron–boson coupling. Strikingly, these replicas are absent in non-superconducting twisted bilayer graphene (TBG) systems, either when MATBG is aligned to hexagonal boron nitride or when TBG deviates from the magic angle. Calculations suggest that the formation of these flat-band replicas in superconducting MATBG are attributed to the strong coupling between flat-band electrons and an optical phonon mode at the graphene K point, facilitated by intervalley scattering. These findings, although they do not necessarily put electron–phonon coupling as the main driving force for the superconductivity in MATBG, unravel the electronic structure inherent in superconducting MATBG, thereby providing crucial information for understanding the unusual electronic landscape from which its superconductivity is derived.

Magic-angle twisted bilayer graphene (MATBG) has attracted extensive research interest owing to its remarkable tunability, offering a versatile platform for the study of strongly correlated electronic phenomena^{1–13}. Many electronic states have been discovered in this low-density electron system, such as superconductivity, strongly correlated insulating states, pseudogap phases, topological phases and orbital magnetism^{12,13}. The intricate interplay of strong electronic Coulomb interactions, which can override kinetic energy in flat-band systems, probably underlies many of these phenomena^{12,13}. Yet, the origin of the unusual superconducting state remains enigmatic, with proposed pairing mechanisms including strong electronic correlations^{14–17}, electron–phonon interactions^{18–22}, spin fluctuations²³ and skyrmions²⁴.

In recent decades, angle-resolved photoemission spectroscopy (ARPES) has emerged as an important tool for investigating quantum materials, enabling the direct visualization of the electronic structure

in momentum space^{25,26}. However, the modest dimensions (usually 1–10 μm) of two-dimensional material devices and the prevalent twist angle inhomogeneity in MATBG devices²⁷ pose challenges for conventional ARPES techniques owing to their limited spatial resolution (usually 50–500 μm). Fortunately, recent advancements in high-throughput X-ray optics²⁸ have empowered us to perform high-quality ARPES measurements with submicrometre spatial precision (μ -ARPES), making it well suited for unravelling the intricate electronic structure in MATBG devices^{29,30}.

In this study, we utilize μ -ARPES measurements to investigate and compare the electronic structures of superconducting MATBG devices (where MATBG is unaligned with its hexagonal boron nitride (hBN) substrate) and non-superconducting twisted bilayer graphene (TBG) systems—both hBN-aligned MATBG and TBGs deviating from the magic angle. Remarkably, in superconducting MATBG devices (unaligned

¹Laboratory for Topological Physics and School of Physical Science and Technology, ShanghaiTech University, Shanghai, People's Republic of China. ²Department of Physics, University of Oxford, Oxford, UK. ³Joseph Henry Laboratories, Princeton University, Princeton, NJ, USA. ⁴Department of Physics, Princeton University, Princeton, NJ, USA. ⁵Department of Chemistry, Emory University, Atlanta, GA, USA. ⁶Materials Department, University of California, Santa Barbara, Santa Barbara, CA, USA. ⁷Institute for Advanced Studies (IAS), Wuhan University, Wuhan, China.

⁸Center for Advanced Quantum Studies, Department of Physics, Beijing Normal University, Beijing, People's Republic of China. ⁹Research Center for Functional Materials, National Institute for Materials Science, Tsukuba, Japan. ¹⁰International Center for Materials Nanoarchitectonics, National Institute for Materials Science, Tsukuba, Japan. ¹¹Advanced Light Source, Lawrence Berkeley National Laboratory, Berkeley, CA, USA. ¹²Department of Physics, Hong Kong University of Science and Technology, Hong Kong, China. ¹³Department of Physics, The Pennsylvania State University, University Park, PA, USA. ¹⁴Donostia International Physics Center, Donostia-San Sebastian, Spain. ¹⁵IKERBASQUE, Basque Foundation for Science, Bilbao, Spain. ¹⁶Department of Physics and Astronomy, Clemson University, Clemson, SC, USA. ¹⁷Present address: Department of Physics, Massachusetts Institute of Technology, Cambridge, MA, USA. ¹⁸Present address: Department of Semiconductor Engineering, Pohang University of Science and Technology (POSTECH), Pohang, Republic of Korea. ¹⁹These authors contributed equally: Cheng Chen, Kevin P. Nuckolls.

[✉]e-mail: yao.wang@emory.edu; yulin.chen@physics.ox.ac.uk

with hBN), a distinct set of replicas of the flat band emerges at higher binding energies. These replicas show robust spectral intensity features that emulate the energy and momentum characteristics of the original flat band. Notably, these replicas manifest across the entire momentum range of the moiré Brillouin zone, maintaining a uniform energy separation of 150 ± 15 meV. In contrast, when subjected to the same experimental conditions, the non-superconducting TBGs—either hBN-aligned MATBG devices or TBGs deviating from the magic angle—do not show flat-band replicas. These experimental findings naturally suggest a strong connection (see Supplementary Information section XIII for more discussions) between the microscopic mechanisms responsible for the formation of flat-band replicas and the occurrence of superconductivity in MATBG.

The observation of replicated bands at higher binding energies in the single-particle ARPES spectrum goes beyond the predictions of non-interacting band theories and often indicates a strongly correlated origin^{31–33}. Through a comprehensive approach involving theoretical analysis and non-perturbative many-body simulations^{19,34}, we found that in superconducting MATBG (hBN unaligned) devices, these observed replicas can be attributed to the strong coupling between flat-band electrons to a transverse optical phonon mode at the graphene K point, facilitated by an intervalley scattering process (discussed below, in Supplementary Information sections VIII–X and in ref. 34). Remarkably, such coupling diminishes in non-superconducting TBG devices, including hBN-aligned MATBG and TBGs deviating from the magic angle (discussed in Supplementary Information sections XI–XII). In summary, our discoveries provide valuable insights into the intricate interplay between flat-band electrons and the bosonic degrees of freedom within MATBG, shedding light on the complex electronic configurations from which superconductivity emerges.

In this study, we first utilized superconducting (hBN unaligned) and non-superconducting (hBN aligned) MATBG devices characterized in a previous investigation¹¹, in which the twist angles and superconducting and spectroscopic properties of these devices were validated through scanning tunnelling microscopy (STM) and scanning tunnelling spectroscopy (STS) analyses (for a concise summary, see Supplementary Information section I). Furthermore, we conducted measurements on non-superconducting TBG devices with twist angles that slightly deviate from the magic angle to enhance the breadth and depth of our comparative analysis.

Measurement schematic and sample geometry

A schematic representation of the μ -ARPES measurement is depicted in Fig. 1a, where a gold pad is connected to the MATBG sample to ensure proper grounding and prevent charge accumulation during measurements. The optical images showing the device geometries for hBN-unaligned and hBN-aligned MATBG samples can be seen in Fig. 1b(i) and Fig. 1c(i), respectively. Notably, the μ -ARPES technique can directly resolve the MATBG band structure, as evidenced in the photoemission intensity maps for each sample, which distinguishes the MATBG regions from the hBN substrate (Fig. 1b(ii)) or single-layer graphene regions (Fig. 1c(ii)).

Although two of the MATBG devices we studied share a nearly identical twist angle of about 1.08° , an optimal value associated with the maximum superconducting transition temperature (T_c) in transport measurements^{1,35}, superconductivity occurs only in the hBN-unaligned device and not in the hBN-aligned devices (see ref. 11 and further details available in Supplementary Information section I). This disparity could be attributed to the influence of distinct moiré potentials stemming from different forms and degrees of coupling between MATBG and its hBN substrate, as illustrated in Fig. 1b(iii) and Fig. 1c(iii). In the unaligned sample (Fig. 1b(iii)), the hBN substrate introduces a high-frequency spatial background to the intrinsic MATBG moiré potential owing to the large angle (about 8°) mismatch between the hBN and MATBG, which

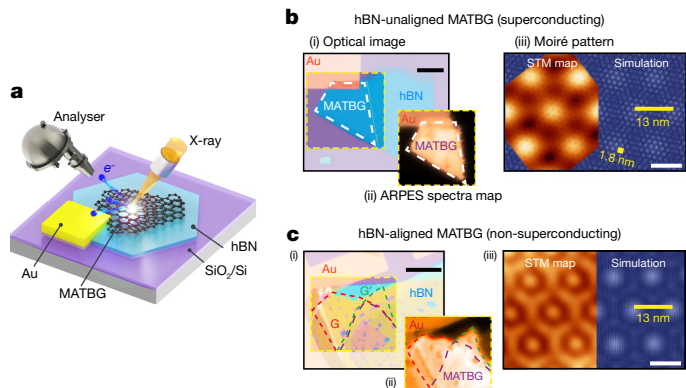


Fig. 1 | μ -ARPES measurement and MATBG device geometries. **a**, Schematic of the μ -ARPES measurement geometry. **b**, Basic characterization of the MATBG (twist angle 1.06°) device A unaligned to its hBN substrate (8° rotational misalignment). (i) Optical image, with the substrate hBN, MATBG region (marked by white dashed lines) and the gold (Au) contact labelled. (ii) ARPES spectral intensity map covering the area enclosed by yellow dashed lines in (i) that highlights the MATBG region of the device. The spectral intensity is integrated within a binding energy of 0.2 eV, visualizing only conductive graphene and gold regions while omitting the hBN and silicon dioxide (SiO_2) regions. (iii) STM topographic image¹⁰ ($V_b = -80$ mV, $I = 300$ pA) and a simulation of the hBN-unaligned MATBG lattice, showing two sets of moiré patterns with different periodicity: the larger one (about 13.3 nm) from the graphene/graphene moiré and the smaller one (about 1.76 nm, marked by the yellow bar) from the graphene/hBN moiré, respectively. **c**, The same as in **b**, but for the MATBG (1.08°) device C aligned with its hBN substrate ($0.5 \pm 0.1^\circ$ rotational misalignment). (i) Optical image with monolayer graphene regions (G and G'; marked by red and green dashed lines) and the MATBG region (marked by purple dashed lines) labelled. The orange-coloured regions of the hBN are the result of two overlapped hBN flakes used to encapsulate this sample's graphite back gate. (ii) ARPES spectral intensity map showing both monolayer graphene and MATBG regions corresponding to regions labelled in (i). (iii) STM topographic image¹¹ ($V_b = -300$ mV, $I = 100$ pA) and lattice simulation, showing a commensurate moiré structure from MATBG and graphene/hBN as both have periodicity around 13 nm. V_b , setpoint sample bias; I , setpoint tunnelling current. Scale bars, 20 μm (**b**(i) and **c**(ii)) and 10 nm (**b**(iii) and **c**(iii)).

does not significantly alter the electronic structure of MATBG. Conversely, in the aligned sample (Fig. 1c(iii)), the moiré periodicity (about 13 nm) introduced by the hBN substrate closely matches that of intrinsic MATBG (13.8 nm) owing to its small twist angle (about 0.5°) relative to the bottom graphene layer. In this aligned sample, the graphene/hBN moiré potential and the resulting C_2 -symmetry-breaking have a profound influence on the electronic structure of pristine MATBG, as is discussed later.

Flat-band replicas in superconducting MATBG

In Fig. 2, we present ARPES data from two superconducting MATBG (hBN-unaligned) devices A and B. The measurements encompass the vicinity of the K points of the individual graphene layers spanning several moiré Brillouin zones (Fig. 2a). A three-dimensional band-structure map of device A is depicted in Fig. 2b, and six representative band dispersion spectra across the moiré Brillouin zones are shown in Fig. 2c. Near the Fermi level (E_F), we observe the flat band of MATBG, which extends throughout the entire moiré Brillouin zone and aligns well with single-particle calculations, as reported previously^{29,30}. Remarkably, we observe previously unresolved replicas of this flat band at higher binding energies (Fig. 2c), which show similar bandwidth, momentum range and spectral distribution to the original flat band.

To provide enhanced clarity, we have captured these features in a series of ARPES dispersion spectra, cutting across the moiré Brillouin

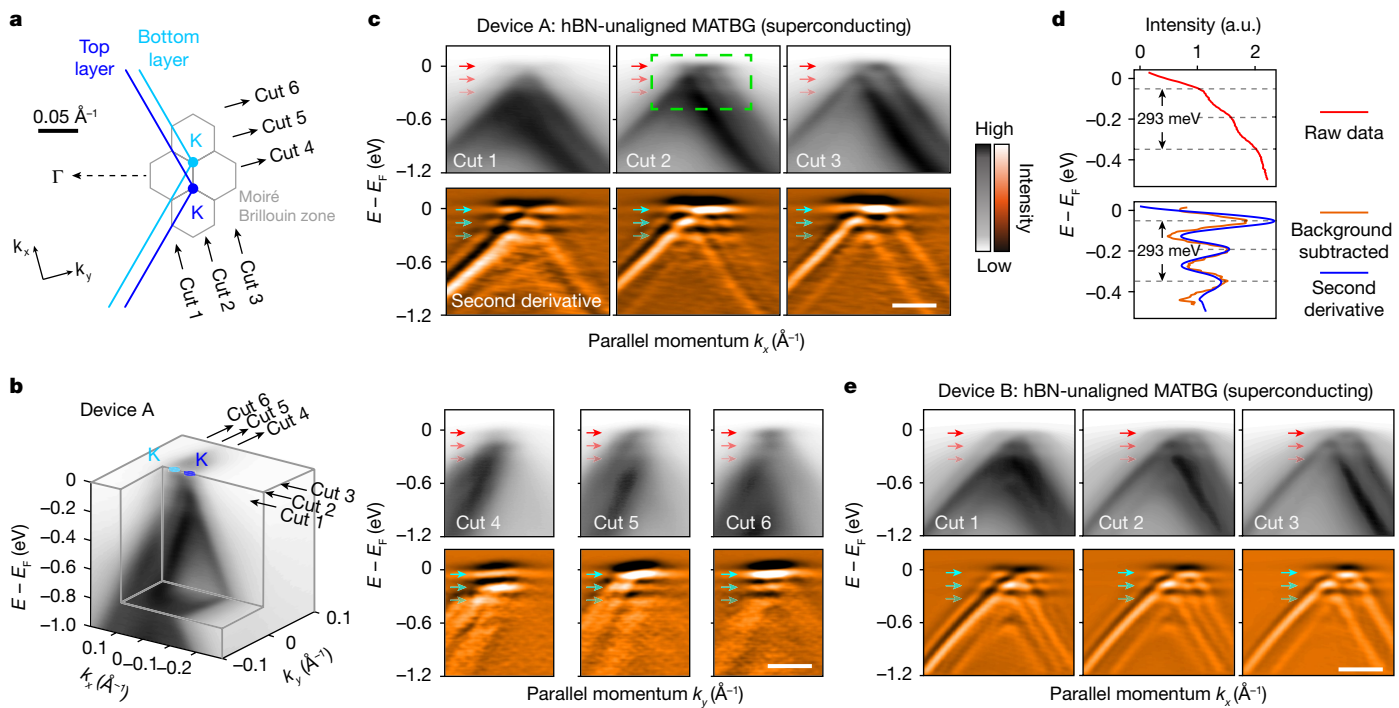


Fig. 2 | Observation of flat-band replicas in superconducting MATBG (hBN unaligned). **a**, Illustration of the MATBG moiré Brillouin zones around the K point of top and bottom monolayer graphene Brillouin zones. The grey lines show the moiré Brillouin zones of MATBG. Cuts 1–6 mark the coordinates of ARPES spectra in **c**. **b**, Three-dimensional intensity plot of ARPES spectra in the vicinity of the graphene K point, presenting an overview of the band structure of MATBG. The ARPES measurements were conducted at room temperature (for details, see Supplementary Information section III). **c**, ARPES dispersion plots taken on superconducting hBN-unaligned MATBG device A (top rows, marked by cuts 1–6 in **a** and **b**) and their associated second partial derivative plots (bottom rows; Methods). The red and cyan arrows in top and bottom rows

highlight the flat band and its first and second replicas, respectively. **d**, Top: integrated ARPES spectra intensity in the green dashed line box in **c**. Bottom: the orange curve represents the same data shown in the top panel with the removal of a smooth background (fourth-degree polynomial). The blue curve represents the integrated intensity of the second-derivative plot within the same green dashed line box. Both the orange and the blue curves show an energy spacing between the flat band and replicas of 150 ± 15 meV. (Details can be found in Supplementary Information section II). **e**, ARPES dispersion plots taken on a second superconducting hBN-unaligned MATBG, device B, where flat band and replicas are observed. (Details can be found in Supplementary Information section III). Scale bars, 0.1\AA^{-1} . a.u., arbitrary units.

zone at different momentum locations (refer to labels 'cut 1' to 'cut 6' in Fig. 2a,b). These observed replicas and the original flat band show a uniform energy separation of 150 ± 15 meV, with intensities diminishing rapidly towards higher binding energies (Fig. 2c,d and detailed in Supplementary Information section II). Similar replica features are also observed in other superconducting MATBG devices (Fig. 2e and Supplementary Information section III for device B; Supplementary Information section V for STS signatures on device F; and Supplementary Information section IV for data from the literature³⁰). These observed replica features cannot be explained by typical band hybridization. First, they consistently manifest at uniform binding energies, unlike in typical band crossing and hybridization processes in which the characteristic energy varies. Second, their presence is not restricted to high-symmetry momenta within the moiré Brillouin zone. Finally, but most importantly, these replicas are absent in non-superconducting TBG devices, a point that is elaborated on in the following.

Absence of replicas in non-superconducting samples

To compare our measurements on superconducting MATBG devices (devices A and B), we also investigated non-superconducting TBG devices, including both hBN-aligned MATBG (device C) and TBGs with the twist angle slightly deviating from the magic angle (devices D and E). As illustrated in Fig. 3a–c, in the hBN-aligned MATBG, we find no indications of the replica features, despite the similarity of its twist angle and strain to the hBN-unaligned MATBG devices shown in Fig. 2. Instead, the band structure of this sample shows characteristic

signatures of band hybridization between the Dirac bands of the two graphene layers, further modified by the commensurate MATBG/hBN moiré potential (Fig. 1b(iii)). It is noteworthy that this distinct electronic structure observed in hBN-aligned MATBG, compared with hBN-unaligned MATBG (for a more comprehensive analysis, refer to Supplementary Information section VI), underscores the significant impact of the moiré-commensurate hBN substrate³⁶, giving rise to unique emergent phenomena, such as the quantum anomalous Hall effect⁵. Moreover, typical signatures of band hybridization are also evident in other non-superconducting TBG devices (devices D and E and also ref. 29) without any discernible signatures of replica band features (Fig. 3d,e).

Strong electron–phonon coupling in MATBG

The observation of replica bands at higher binding energies in single-particle ARPES spectra typically signifies the presence of strong electron–boson coupling in the system^{31–33}. In TBG, the concurrent emergence of these replica flat bands and superconductivity further indicates a shared underlying mechanism. This connection closely parallels the observation of shake-off replica bands in FeSe/SrTiO₃ (refs. 31,37,38), which probably arise from the strong coupling of electrons in monolayer FeSe to an optical phonon mode in SrTiO₃. This strong electron–phonon coupling (EPC) was proposed to account for the much-enhanced superconducting transition temperature in this composite system compared with FeSe alone^{31,37,38}. Despite the presence of various bosonic modes in MATBG, few are consistent with

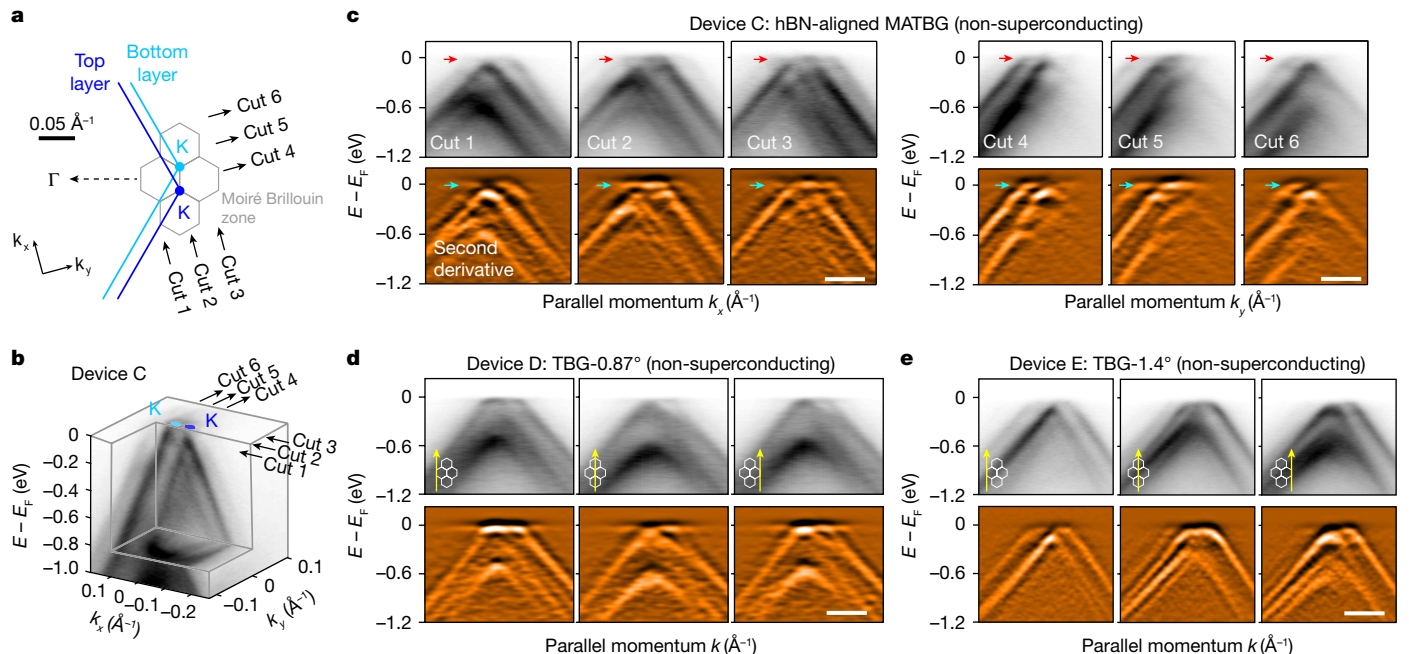


Fig. 3 | Absence of flat-band replicas in non-superconducting TBG devices.

a, Illustration of the MATBG moiré Brillouin zones around the K point of top and bottom monolayer graphene. The grey lines show the moiré Brillouin zones of MATBG. Cuts 1–6 mark the coordinates of ARPES spectra in **c**.

b, Three-dimensional intensity plot of ARPES spectra in the vicinity of the graphene K point, presenting an overview of the band structure of hBN-aligned MATBG. Here the electronic structure of MATBG is modified by the commensurate alignment of hBN compared with the unaligned case illustrated in Fig. 2.

(A detailed comparison can be found in Supplementary Information section VI).

c, ARPES dispersion plots and second-derivative plots taken along the same momentum directions (marked in **a** and **b**) as those in Fig. 2 for the hBN-unaligned MATBG sample. The flat band is labelled by red and cyan arrows. No signs of replicas of the flat band were observed, in contrast to the data shown in Fig. 2. **d,e**, ARPES dispersion plots (direction with respect to moiré Brillouin zones in **a** is illustrated in the bottom-left corner) and second-derivative plots taken on the TBG devices with a twist angle of 0.87° (**d**) and 1.4° (**e**), smaller or larger than the magic region. No signature of flat-band replicas is evidenced. Scale bars, 0.1 Å⁻¹.

our observations. For instance, collective spin fluctuations, which couple with electrons to form magnetic polarons, can be ruled out, as they would yield unevenly spaced replica bands³⁹. Plasmons, which couple with electrons to form plasmarons, are also unlikely candidates because the energy separation of the resulting replicas would be well below 150 meV (refs. 40,41) owing to the low carrier density in intrinsic MATBG/hBN¹. In contrast, phonons, which couple with electrons to form polarons, are expected to have mode energies around 150 meV, matching the energy spacing of the observed replicas, and thus stand as the most plausible origin^{31–33,37,38}.

Given the negligible electronic kinetic energy of the flat bands in MATBG (approximately 10–15 meV) compared with the large mode energy (approximately 150 meV), we initially examined the intrinsic phonon spectra of graphene, without considering the renormalization caused by polaronic dressing. To induce replica features in both moiré Brillouin zones, the relevant phonon modes should reside around the Γ or K (K') point in the original graphene Brillouin zone, allowing them to couple with the corresponding intra- or intervalley electron-hole processes, respectively. In Fig. 4a, we emphasize three phonon branches (distinguished by green, red and blue colours) with energies around 150 meV near the K point, indicating their potential to mediate intervalley EPC. Notably, our frozen-phonon calculations reveal that the in-plane transverse optical (red line) mode shows the highest EPC strength dominant over the other two (in-plane longitudinal optical and in-plane longitudinal acoustic) relevant modes (as detailed in Fig. 4b and Supplementary Information sections VII and VIII). This substantial difference in EPC strength is attributed to the symmetry of flat-band wavefunctions and two-centre approximation³⁴, consistent with previous findings^{42,43}.

The in-plane transverse optical phonon mode scatters flat-band electrons between the moiré Brillouin zones at the K and K' points (depicted

in Fig. 4c), resulting in a series of evenly spaced replica bands akin to those produced by forward-scattering phonons in each moiré Brillouin zone. The observed ARPES spectra can be well reproduced (Fig. 4d, with details in Methods and Supplementary Information section IX), with the energy separation determined by the phonon energy, which significantly surpasses the electronic bandwidth of about 15 meV (refs. 31–33).

Using the same EPC model, we further simulate the ARPES spectrum with the presence of valley-dependent potentials induced by the aligned hBN substrate. As shown in Fig. 4e, the polaronic replicas are significantly suppressed with the presence of the hBN potential denoted as Δ (for details, see Supplementary Information section X), in agreement with our experimental observation. In addition, to address the disappearance of polaronic replicas at larger and smaller twist angles in TBG, we conducted simulations to explore the relative replica intensity at varying bandwidths. As shown in Fig. 4f, the Poisson factor experiences a pronounced reduction as the bandwidth increases from the flat-band limit ($\omega = 0$) to finite values. Such a suppression reflects a similar mechanism to that influenced by the hBN potential Δ , highlighting the competition between the single-particle electronic Hamiltonian and the valley-crossing EPC. This competition originates from the non-commuting nature of EPC matrices with the hBN potential or kinetic energy terms and reveals a universal phenomenon in materials with strong EPC (for detailed discussions, refer to Supplementary Information sections X–XII).

Discussion and conclusion

We now discuss how this experimentally identified EPC may further contribute to electronic pairing in MATBG. Our raw estimation indicates that MATBG lies in the strong-coupling regime (for details and an explanation of strong coupling, see Supplementary Information section VIII),

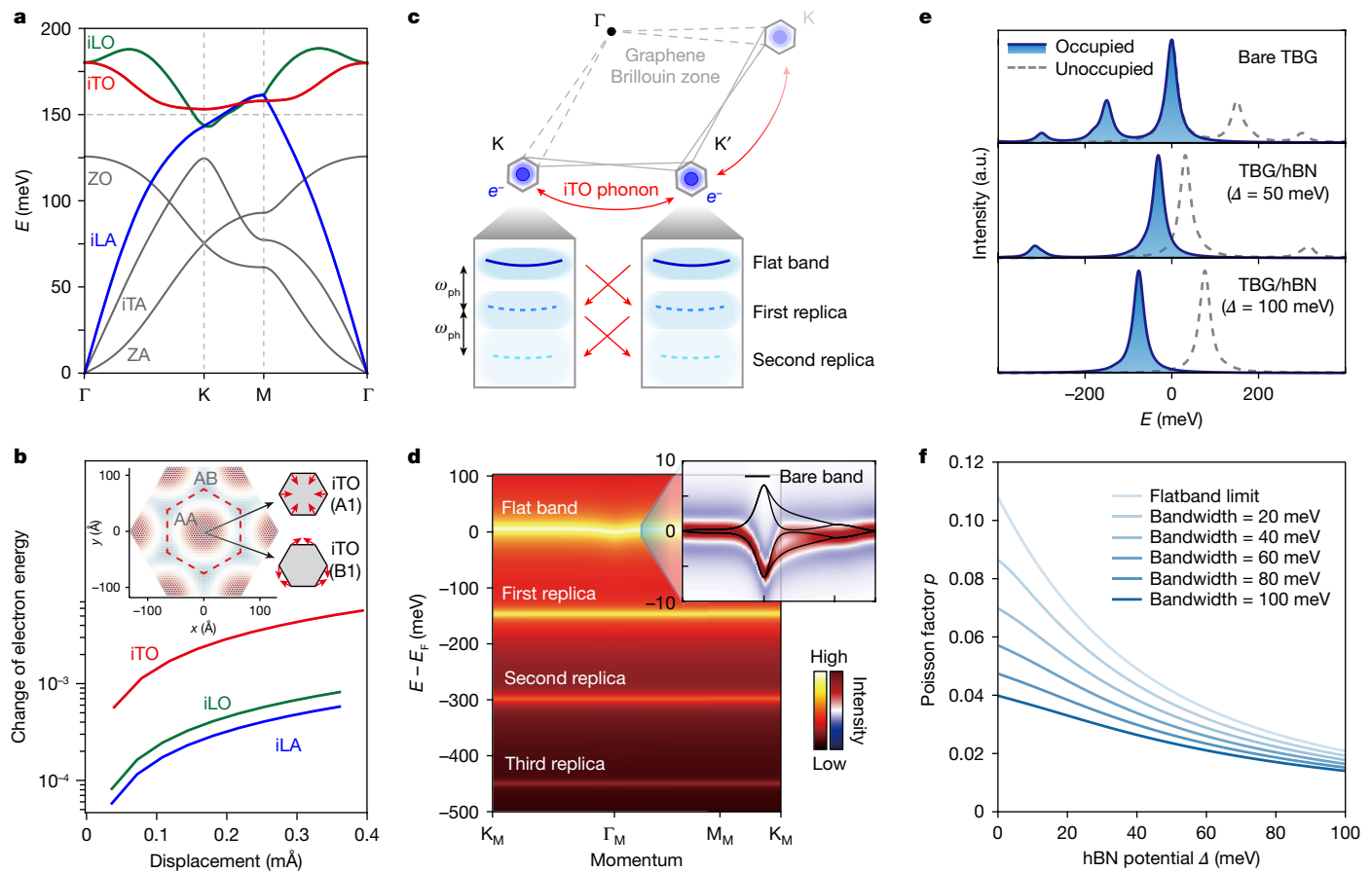


Fig. 4 | Intervalley EPC in MATBG. **a**, Calculated phonon spectra of single-layer graphene. Three phonon modes, in-plane longitudinal optical mode (iLO), in-plane transverse optical mode (iTO), in-plane longitudinal acoustic mode (iLA), with approximately 150 meV energy around the K point are highlighted. iTA is in-plane transverse acoustic mode, ZO is out-of-plane optical mode and ZA is out-of-plane acoustic mode. **b**, Calculated effective EPC strength of iTO, iLO and iLA phonon modes as a function of average lattice distortion. The EPC strength of the iTO mode is almost an order of magnitude larger than the other two modes. Inset: real-space lattice distortion magnitude induced by A1 and B1 modes of iTO phonons, which peaks at the AA-stacking regions and diminishes at the AB-stacking regions. (Details can be found in Supplementary Information section VIII). **c**, Schematic of the intervalley EPC in MATBG. Flat-band electrons from two moiré Brillouin zones at the K and K' points are exchanged through

the scattering of iTO phonons, which generates shake-off replica bands separated by energy intervals of the iTO phonon energy ω_{ph} . **d**, Simulated photoemission spectra of the flat band and replicas. The top-right panel shows the zoomed-in second-derivative spectra of the flat bands, where the solid lines are the calculated dispersion of bare bands without EPC. (Details can be found in Supplementary Information section IX). **e**, Electron removal (solid blue line, occupied states) and addition (dashed grey line, unoccupied states) spectral function obtained with the presence of band inversion induced by the hBN substrate potential Δ . The flat-band replica is suppressed with increasing Δ (Supplementary Information section XII). **f**, The replica Poisson factor ρ , which reflects the relative intensity of ARPES replica, as a function of both hBN substrate potential Δ and the flat-band bandwidth w (Supplementary Information sections X and XI).

consistent with the observation of a pseudogap above T_c (ref. 11). We emphasize that the involvement of phonons does not necessarily lead to conventional s-wave superconductivity, given the topological nature of multiple flat bands³⁴. Previous studies have shown that intervalley EPC can facilitate d-wave pairing in the intra-Chern-band channel^{19,34,44}, which opens the possibility of various pairing scenarios, including time-reversal breaking chiral d-wave pairing or gapless nematic d-wave pairing⁴⁵, with the latter consistent with previous STS observations of a nodal tunnelling gap¹¹.

Owing to the intervalley nature of the EPC, a local Coulomb interaction in the chiral limit commutes with the EPC terms. As a result, the polaronic replicas induced by EPC are not affected by the presence of any local Coulomb interactions (Supplementary Information section XII). The coexistence of both strong EPC and Coulomb repulsions is anticipated to introduce further complexity to the pairing symmetry in MATBG and may collaborate in stabilizing superconductivity, as recently discussed for cuprates^{46–48}. At low temperatures, these pairing properties would be reflected by electronic properties within the energy window of each replica. Unfortunately, this range lies beyond the

reach of the current μ -ARPES set-up owing to the temperature limitation (about 20 K) and resolution constraints (about 20 meV). However, the nature of electronic many-body states should not affect the quantification of polaronic replica features at the energy scale of 150 meV, thus is unlikely to substantially alter the interpretation presented above.

Our findings underscore the importance, although not necessarily the dominating role, of intervalley phonon modes in superconducting MATBG, which act to dress the electronic states of the flat bands in ways that closely resemble those found in iron-based high- T_c superconductors^{31,37,38}. Going forward, we anticipate that forthcoming experimental endeavours will provide additional insights into the connection between the microscopic mechanisms driving replica flat bands and those underpinning superconductivity in twisted graphene systems. For instance, similar replica flat bands may emerge in superconducting magic-angle twisted trilayer graphene⁴⁹, whereas they may be absent in non-superconducting twisted monolayer–bilayer graphene⁵⁰. Furthermore, we expect that the distinctive capabilities of μ -ARPES (and more advanced nano-ARPES) will find widespread use in investigating strong correlation effects in moiré systems.

Online content

Any methods, additional references, Nature Portfolio reporting summaries, source data, extended data, supplementary information, acknowledgements, peer review information; details of author contributions and competing interests; and statements of data and code availability are available at <https://doi.org/10.1038/s41586-024-08227-w>.

1. Cao, Y. et al. Unconventional superconductivity in magic-angle graphene superlattices. *Nature* **556**, 43–50 (2018).
2. Cao, Y. et al. Correlated insulator behaviour at half-filling in magic-angle graphene superlattices. *Nature* **556**, 80–84 (2018).
3. Lu, X. et al. Superconductors, orbital magnets and correlated states in magic-angle bilayer graphene. *Nature* **574**, 653–657 (2019).
4. Yankowitz, M. et al. Tuning superconductivity in twisted bilayer graphene. *Science* **363**, 1059–1064 (2019).
5. Serlin, M. et al. Intrinsic quantized anomalous Hall effect in a moiré heterostructure. *Science* **367**, 900–903 (2020).
6. Sharpe, A. L. et al. Emergent ferromagnetism near three-quarters filling in twisted bilayer graphene. *Science* **365**, 605–608 (2019).
7. Kerelsky, A. et al. Maximized electron interactions at the magic angle in twisted bilayer graphene. *Nature* **572**, 95–100 (2019).
8. Xie, Y. et al. Spectroscopic signatures of many-body correlations in magic-angle twisted bilayer graphene. *Nature* **572**, 101–105 (2019).
9. Nuckolls, K. P. et al. Strongly correlated Chern insulators in magic-angle twisted bilayer graphene. *Nature* **588**, 610–615 (2020).
10. Wong, D. et al. Cascade of electronic transitions in magic-angle twisted bilayer graphene. *Nature* **582**, 198–202 (2020).
11. Oh, M. et al. Evidence for unconventional superconductivity in twisted bilayer graphene. *Nature* **600**, 240–245 (2021).
12. Andrei, E. Y. & MacDonald, A. H. Graphene bilayers with a twist. *Nat. Mater.* **19**, 1265–1275 (2020).
13. Balents, L., Dean, C. R., Efetov, D. K. & Young, A. F. Superconductivity and strong correlations in moiré flat bands. *Nat. Phys.* **16**, 725–733 (2020).
14. Dodaro, J. F., Kivelson, S. A., Schattner, Y., Sun, X. Q. & Wang, C. Phases of a phenomenological model of twisted bilayer graphene. *Phys. Rev. B* **98**, 075154 (2018).
15. Xu, C. & Balents, L. Topological superconductivity in twisted multilayer graphene. *Phys. Rev. Lett.* **121**, 087001 (2018).
16. Guo, H., Zhu, X., Feng, S. & Scalettar, R. T. Pairing symmetry of interacting fermions on a twisted bilayer graphene superlattice. *Phys. Rev. B* **97**, 235453 (2018).
17. Guinea, F. & Walet, N. R. Electrostatic effects, band distortions, and superconductivity in twisted graphene bilayers. *Proc. Natl Acad. Sci. USA* **115**, 13174–13179 (2018).
18. Lian, B., Wang, Z. & Bernevig, B. A. Twisted bilayer graphene: a phonon-driven superconductor. *Phys. Rev. Lett.* **122**, 257002 (2019).
19. Wu, F., MacDonald, A. H. & Martin, I. Theory of phonon-mediated superconductivity in twisted bilayer graphene. *Phys. Rev. Lett.* **121**, 257001 (2018).
20. Peltonen, T. J., Oja-Järvi, R. & Heikkilä, T. T. Mean-field theory for superconductivity in twisted bilayer graphene. *Phys. Rev. B* **98**, 220504 (2018).
21. Choi, Y. W. & Choi, H. J. Strong electron–phonon coupling, electron–hole asymmetry, and nonadiabaticity in magic-angle twisted bilayer graphene. *Phys. Rev. B* **98**, 241412 (2018).
22. Choi, Y. W. & Choi, H. J. Dichotomy of electron–phonon coupling in graphene moiré flat bands. *Phys. Rev. Lett.* **127**, 167001 (2021).
23. Liu, C. C., Zhang, L. D., Chen, W. Q. & Yang, F. Chiral spin density wave and d+id superconductivity in the magic-angle-twisted bilayer graphene. *Phys. Rev. Lett.* **121**, 217001 (2018).
24. Khalaf, E., Chatterjee, S., Bultinck, N., Zaletel, M. P. & Vishwanath, A. Charged skyrmions and topological origin of superconductivity in magic-angle graphene. *Sci. Adv.* **7**, eabf5299 (2021).
25. Sobota, J. A., He, Y. & Shen, Z.-X. Angle-resolved photoemission studies of quantum materials. *Rev. Mod. Phys.* **93**, 025006 (2021).
26. Yang, H. et al. Visualizing electronic structures of quantum materials by angle-resolved photoemission spectroscopy. *Nat. Rev. Mater.* **3**, 341–353 (2018).
27. Uri, A. et al. Mapping the twist-angle disorder and Landau levels in magic-angle graphene. *Nature* **581**, 47–52 (2020).
28. Koch, R. J. et al. Nano focusing of soft X-rays by a new capillary mirror optic. *Synchrotron Radiat. News* **31**, 50–52 (2018).
29. Lisi, S. et al. Observation of flat bands in twisted bilayer graphene. *Nat. Phys.* **17**, 189–193 (2021).
30. Utama, M. I. B. et al. Visualization of the flat electronic band in twisted bilayer graphene near the magic angle twist. *Nat. Phys.* **17**, 184–188 (2021).
31. Lee, J. J. et al. Interfacial mode coupling as the origin of the enhancement of T_c in FeSe films on SrTiO_3 . *Nature* **515**, 245–248 (2014).
32. Wang, Z. et al. Tailoring the nature and strength of electron–phonon interactions in the SrTiO_3 (001) 2D electron liquid. *Nat. Mater.* **15**, 835–839 (2016).
33. Chen, C. et al. Emergence of interfacial polarons from electron–phonon coupling in graphene/h-BN van der Waals heterostructures. *Nano Lett.* **18**, 1082–1087 (2018).
34. Liu, C.-X., Chen, Y., Yazdani, A. & Andrei Bernevig, B. Electron–K-phonon interaction in twisted bilayer graphene. *Phys. Rev. B* **110**, 045133 (2024).
35. Saito, Y., Ge, J., Watanabe, K., Taniguchi, T. & Young, A. F. Independent superconductors and correlated insulators in twisted bilayer graphene. *Nat. Phys.* **16**, 926–930 (2020).
36. Cea, T., Pantaleón, P. A. & Guinea, F. Band structure of twisted bilayer graphene on hexagonal boron nitride. *Phys. Rev. B* **102**, 155136 (2020).
37. Song, Q. et al. Evidence of cooperative effect on the enhanced superconducting transition temperature at the FeSe/ SrTiO_3 interface. *Nat. Commun.* **10**, 758 (2019).
38. Zhang, C. et al. Ubiquitous strong electron–phonon coupling at the interface of FeSe/ SrTiO_3 . *Nat. Commun.* **8**, 14468 (2017).
39. Martinez, G. & Horsch, P. Spin polarons in the t–J model. *Phys. Rev. B* **44**, 317–331 (1991).
40. Bostwick, A. et al. Observation of plasmarons in quasi-free-standing doped graphene. *Science* **328**, 999–1002 (2010).
41. Zhang, H. et al. Experimental evidence of plasmarons and effective fine structure constant in electron-doped graphene/h-BN heterostructure. *npj Quantum Mater.* **6**, 83 (2021).
42. Angelis, M., Tosatti, E. & Fabrizio, M. Valley Jahn–Teller effect in twisted bilayer graphene. *Phys. Rev. X* **9**, 041010 (2019).
43. Angelis, M. & Fabrizio, M. Jahn–Teller coupling to moiré phonons in the continuum model formalism for small-angle twisted bilayer graphene. *Eur. Phys. J. Plus* **135**, 630 (2020).
44. Wang, Y. et al. Molecular pairing in twisted bilayer graphene superconductivity. *Phys. Rev. Lett.* **133**, 146001 (2024).
45. Yu, J. et al. Euler obstructed Cooper pairing in twisted bilayer graphene: nematic nodal superconductivity and bounded superfluid weight. *Phys. Rev. B* **105**, 104515 (2022).
46. Lanzara, A. et al. Evidence for ubiquitous strong electron–phonon coupling in high-temperature superconductors. *Nature* **412**, 510–514 (2001).
47. Reznik, D. et al. Electron–phonon coupling reflecting dynamic charge inhomogeneity in copper oxide superconductors. *Nature* **440**, 1170–1173 (2006).
48. He, Y. et al. Rapid change of superconductivity and electron–phonon coupling through critical doping in Bi-2212. *Science* **362**, 62–65 (2018).
49. Park, J. M., Cao, Y., Watanabe, K., Taniguchi, T. & Jarillo-Herrero, P. Tunable strongly coupled superconductivity in magic-angle twisted trilayer graphene. *Nature* **590**, 249–255 (2021).
50. Polshyn, H. et al. Electrical switching of magnetic order in an orbital Chern insulator. *Nature* **588**, 66–70 (2020).

Publisher's note Springer Nature remains neutral with regard to jurisdictional claims in published maps and institutional affiliations.



Open Access This article is licensed under a Creative Commons Attribution 4.0 International License, which permits use, sharing, adaptation, distribution and reproduction in any medium or format, as long as you give appropriate credit to the original author(s) and the source, provide a link to the Creative Commons licence, and indicate if changes were made. The images or other third party material in this article are included in the article's Creative Commons licence, unless indicated otherwise in a credit line to the material. If material is not included in the article's Creative Commons licence and your intended use is not permitted by statutory regulation or exceeds the permitted use, you will need to obtain permission directly from the copyright holder. To view a copy of this licence, visit <http://creativecommons.org/licenses/by/4.0/>.

© The Author(s) 2024

Methods

Sample fabrication

MATBG devices A, B and C are devices B, F and C from ref. 11 (the full description of the fabrication procedure can be found in this reference). In brief, devices were fabricated using a ‘tear-and-stack’ method⁵¹ in which a single graphene sheet is torn in half by van der Waals interaction with hBN. The two halves were rotated relative to each other and stacked to form MATBG. Graphene, graphite (in the aligned device) and hBN were picked up with polyvinyl alcohol. Then, to flip the heterostructure upside down, the heterostructure was pressed against an intermediate structure consisting of polymethyl methacrylate/transparent tape/Sylgard 184, and the polyvinyl alcohol was dissolved by water injection. The heterostructure was then transferred to a SiO₂/Si chip with pre-patterned titanium/gold electrodes. Residual polymer was dissolved in dichloromethane, water, acetone and isopropyl alcohol. These chips were annealed in ultrahigh vacuum at 170 °C overnight and at 400 °C for 2 h in previous STM and STS measurements¹¹. The other devices shared a similar fabrication and preparation method.

Spatial- and angle-resolved photoemission spectroscopy

Synchrotron-based μ -ARPES measurements were performed at Beamline 7.0.2 (MAESTRO) of the Advanced Light Source, USA and Beamline 07U of the Shanghai Synchrotron Radiation Facility (SSRF), China. The samples were annealed in ultrahigh vacuum at 300 °C for 3 h and measured under ultrahigh vacuum below 3×10^{-11} torr. The photon energy of the incident beam was 95 eV and the measurement was performed at room temperature. Data were collected using an R4000 analyser upgraded with deflectors (Advanced Light Source) and a DA30 analyser (SSRF). The incoming photon beam was focused down to a 2- μm spot size by using a capillary mirror²⁸ and a 1- μm spot size using a Fresnel zone plate (SSRF). The total energy and angle resolutions were 20 meV and 0.1°, respectively.

Laplacian (sum of second partial derivatives) plots were used to highlight the non-dispersive bands, as presented in Figs. 2 and 3. These plots were generated by summing the second partial derivatives of the original ARPES spectra along both axes in pixel units, then transforming them into energy and momentum space.

Model calculation

Estimation of EPC. We adopted the following non-interacting-electron tight-binding Hamiltonian to calculate the electronic structure and EPC of MATBG

$$H = - \sum_{i\alpha, j\beta} t(\mathbf{R}_{i\alpha} - \mathbf{R}_{j\beta}) c_{i\alpha}^\dagger c_{j\beta} \quad (1)$$

where $c_{i\alpha}^\dagger$ and $c_{j\beta}^\dagger$ are creation and annihilation operators for the p_z orbital of the $i\alpha/j\beta$ carbon atom in the i/j th moiré superlattice (α and β are joint indices for sublattices and layers), and \mathbf{R} is the corresponding atomic coordinate. The impact of atomic coordinates on the hopping parameter t is approximated by the Slater–Koster formula, whose dependence on atomic coordinates sets the stage for the EPC estimation. The Slater–Koster parameters are specified in Supplementary Information section VII.

To evaluate the coupling in the mini-Brillouin zone, we further projected the coupling matrix using the truncated atomic plane wave (TAPW) method^{43,52}. Thus, a moiré phonon near the Γ_M point can be approximated by in-plane transverse optical/in-plane longitudinal acoustic/in-plane longitudinal optical phonons at graphene K/K' points (see Supplementary Information section VIII for details). We set the moiré phonon energy $\omega_0 = 150$ meV, the mass of carbon atoms $m_c = 2.0 \times 10^{-26}$ kg, and the characteristic phonon length $l_p = \sqrt{\hbar/(2m_c\omega_0)} = 34.0$ mÅ. The TAPW electrons and projected EPC constitute the model Hamiltonian for the TBG system

$$H = \sum_{\bar{\mathbf{k}}\sigma} \mathbf{c}_{\bar{\mathbf{k}}\sigma}^{(\text{TAPW})\dagger} h_{\bar{\mathbf{k}}} \mathbf{c}_{\bar{\mathbf{k}}\sigma}^{(\text{TAPW})} - \frac{1}{\sqrt{N_m}} \sum_{\bar{\mathbf{k}}\sigma\bar{\mathbf{q}}v} \mathbf{c}_{\bar{\mathbf{k}}+\bar{\mathbf{q}}\sigma}^{(\text{TAPW})\dagger} M_{\bar{\mathbf{q}}v} \mathbf{c}_{\bar{\mathbf{k}}\sigma}^{(\text{TAPW})} (a_{\bar{\mathbf{q}}v} + a_{-\bar{\mathbf{q}}v}^\dagger) + \sum_{\bar{\mathbf{q}}v} \omega_0 a_{\bar{\mathbf{q}}v}^\dagger a_{\bar{\mathbf{q}}v} \quad (2)$$

where $\mathbf{c}_{\bar{\mathbf{k}}\sigma}^{(\text{TAPW})}$ is the column vector of electron annihilation operators with moiré momentum $\bar{\mathbf{k}}$ and spin σ in the TAPW basis and $h_{\bar{\mathbf{k}}}$ is the electronic hopping matrix for a specific moiré momentum $\bar{\mathbf{k}}$. The size of its moiré mini-Brillouin zone is denoted as N_m to distinguish from the system size N . For folded phonon branches, $a_{\bar{\mathbf{q}}v}$ is the annihilation operator with moiré momentum $\bar{\mathbf{q}}$ and v labels the index of branches. The average distance between phonons and electrons is small compared with the moiré length scale. Therefore, the coupling matrix $M_{\bar{\mathbf{q}}v}$ can be estimated by the momentum-independent M_0 , which can be evaluated by the frozen-phonon calculations.

As the experimentally relevant electrons lie in low-energy flat bands, we further project the TAPW orbitals onto the four flat-band orbitals, which can be expressed as the projection operator $\mathbf{c}_{\bar{\mathbf{k}}\sigma}^{(\text{flat})} = P_{\bar{\mathbf{k}}}^\dagger \mathbf{c}_{\bar{\mathbf{k}}\sigma}^{(\text{TAPW})}$, where P is the flat-band projection operator. In the projected Hamiltonian, the EPC matrix becomes a 4×4 -dimensional $\tilde{M}_{\bar{\mathbf{k}}}(\bar{\mathbf{q}}) = P_{\bar{\mathbf{k}}+\bar{\mathbf{q}}}^\dagger M_0 P_{\bar{\mathbf{k}}}$. On the basis of its numerical distribution (Supplementary Information section VIII), we find that $\tilde{M}_{\bar{\mathbf{k}}}(\bar{\mathbf{q}})$ can be approximated by $Q_{\bar{\mathbf{k}}+\bar{\mathbf{q}}} g_{\bar{\mathbf{q}}} \eta Q_{\bar{\mathbf{k}}}^\dagger$, where Q is the similarity transformation, g is the coupling strength and η is a constant diagonal matrix. Thus, the projected Hamiltonian can be written in an EPC-diagonal basis

$$H_{\text{flat-band}} = \sum_{\bar{\mathbf{k}}\sigma} \mathbf{d}_{\bar{\mathbf{k}}\sigma}^\dagger Q_{\bar{\mathbf{k}}}^\dagger \varepsilon_{\bar{\mathbf{k}}} Q_{\bar{\mathbf{k}}} \mathbf{d}_{\bar{\mathbf{k}}\sigma} - \frac{1}{\sqrt{N_m}} \sum_{\bar{\mathbf{k}}\sigma\bar{\mathbf{q}}v} g_{\bar{\mathbf{q}}} \mathbf{d}_{\bar{\mathbf{k}}+\bar{\mathbf{q}}\sigma}^\dagger \eta \mathbf{d}_{\bar{\mathbf{k}}\sigma} (a_{\bar{\mathbf{q}}v} + a_{-\bar{\mathbf{q}}v}^\dagger) + \sum_{\bar{\mathbf{q}}v} \omega_0 a_{\bar{\mathbf{q}}v}^\dagger a_{\bar{\mathbf{q}}v} \quad (3)$$

where $\mathbf{d}_{\bar{\mathbf{k}}\sigma} = Q_{\bar{\mathbf{k}}}^\dagger \mathbf{c}_{\bar{\mathbf{k}}\sigma}^{(\text{flat})}$ and the diagonal matrix $\varepsilon_{\bar{\mathbf{k}}}$ represents the energy of the flat bands.

ARPES spectral simulation for TBG. The strong EPC for the flat-band electrons leads to non-perturbative polaronic dressing effects. We consider the Lang–Firsov transformation for the coupled Hamiltonian

$$U_{\text{LF}} = e^{-\frac{1}{\sqrt{N_m}\omega_0} \sum_{\bar{\mathbf{R}}\sigma\bar{\mathbf{q}}v} e^{-i\bar{\mathbf{R}}\cdot\bar{\mathbf{q}}} g_{\bar{\mathbf{q}}} \mathbf{d}_{\bar{\mathbf{R}}\sigma}^\dagger \eta \mathbf{d}_{\bar{\mathbf{R}}\sigma} (a_{\bar{\mathbf{q}}v} - a_{-\bar{\mathbf{q}}v}^\dagger)} \quad (4)$$

where $\mathbf{d}_{\bar{\mathbf{R}}\sigma}$ is the real-space annihilation operator of electron in the EPC-diagonal basis. Owing to the separation of energy scales for electrons and phonons, we can employ the polaron ansatz for the ground-state wavefunction $|\Psi_G\rangle = U_{\text{LF}}^\dagger |\Psi_e\rangle \otimes |\Psi_{\text{ph}}\rangle$, where $|\Psi_e\rangle$ and $|\Psi_{\text{ph}}\rangle$ are the electronic and phononic wavefunctions. Moreover, as both the transformed coupling strength $g_{\bar{\mathbf{q}}}$ and temperature are much less than the phonon energy $\omega_0 = 150$ meV, we further assume that the $|\Psi_{\text{ph}}\rangle$ can be approximated by a vacuum state $|0_{\text{ph}}\rangle$. Thus, the electronic part $|\Psi_e\rangle$ is determined by an effective Hamiltonian

$$\langle 0_{\text{ph}} | U_{\text{LF}} H U_{\text{LF}}^\dagger | 0_{\text{ph}} \rangle = \sum_{\bar{\mathbf{R}}\bar{\mathbf{R}}'\sigma} \mathbf{d}_{\bar{\mathbf{R}}\sigma}^\dagger \langle 0_{\text{ph}} | h_{\bar{\mathbf{R}}\bar{\mathbf{R}}'}^* | 0_{\text{ph}} \rangle \mathbf{d}_{\bar{\mathbf{R}}'\sigma} - \sum_{\bar{\mathbf{R}}\bar{\mathbf{R}}'\sigma\bar{\mathbf{q}}v} \frac{N_v |g_{\bar{\mathbf{q}}}|^2}{N_m \omega_0} e^{i(\bar{\mathbf{R}}'\cdot\bar{\mathbf{R}})\cdot\bar{\mathbf{q}}} (\mathbf{d}_{\bar{\mathbf{R}}\sigma}^\dagger \eta \mathbf{d}_{\bar{\mathbf{R}}\sigma}) (\mathbf{d}_{\bar{\mathbf{R}}'\sigma}^\dagger \eta \mathbf{d}_{\bar{\mathbf{R}}'\sigma}) \quad (5)$$

The $h_{\bar{\mathbf{R}}\bar{\mathbf{R}}'}^*$ is the phonon-dressed electronic hopping matrix, whose specific form is shown in Supplementary Information section X. In the flat-band limit of TBG, this matrix is close to identity and, therefore, is irrelevant in determining the polaronic dressing. The ground state of the above equation determines the $|\Psi_e\rangle$ in $|\Psi_G\rangle$.

The photoemission spectrum also involves excited states (denoted as $|\Phi\rangle$)

$$A(\bar{\mathbf{k}}, \omega) = \text{Im} \left\{ \frac{1}{N_m} \sum_{\bar{\mathbf{R}} \bar{\mathbf{R}}} e^{-i(\bar{\mathbf{R}} - \bar{\mathbf{R}}') \cdot \bar{\mathbf{k}}} \sum_{\sigma, \Phi} \langle \Psi_G | c_{\bar{\mathbf{R}} \sigma a}^{\dagger(\text{flat})} | \Phi \rangle \langle \Phi | c_{\bar{\mathbf{R}}' \sigma a}^{(\text{flat})} | \Psi_G \rangle \right. \\ \left. \frac{1}{\omega - i\Gamma + E_\Phi - E_G} \right\} \quad (6)$$

where Γ is the Lorentzian broadening. With the aforementioned ground-state ansatz, the intensity of the M th replica peak is explicitly determined as

$$\frac{1}{M!} \exp \left(- \sum_{\bar{\mathbf{q}}} \frac{N_\nu |g_{\bar{\mathbf{q}}}|^2}{N_m \omega_0^2} \right) \left(\sum_{\bar{\mathbf{q}}} \frac{N_\nu |g_{\bar{\mathbf{q}}}|^2}{N_m \omega_0^2} e^{i\bar{\mathbf{R}} \cdot \bar{\mathbf{q}}} \right)^M \quad (7)$$

It follows a Poisson distribution with the factor $\sum_{\bar{\mathbf{q}}} \frac{N_\nu |g_{\bar{\mathbf{q}}}|^2}{N_m \omega_0^2} \approx 0.11$, according to the frozen-phonon simulations. Focusing on the relative intensity of replica features and ignoring the interacting nature of electrons inside each replica, we produce the spectral simulation in Fig. 4d.

Variational non-Gaussian ansatz for more general models. The Lang–Firsov transformation is suitable for the flat-band TBG model. The experiments presented in this paper also include TBG under more complicated conditions, including with hBN substrates and finite bandwidth away from the magic angle. These generalized cases can be modelled in the form of

$$H = \sum_{\bar{\mathbf{k}}\sigma} \mathbf{d}_{\bar{\mathbf{k}}\sigma}^\dagger h_{\bar{\mathbf{k}}} \mathbf{d}_{\bar{\mathbf{k}}\sigma} - \frac{1}{\sqrt{N_m}} \sum_{\bar{\mathbf{k}}\sigma} \mathbf{d}_{\bar{\mathbf{k}}+\bar{\mathbf{q}}\sigma}^\dagger M_{\bar{\mathbf{q}}} \mathbf{d}_{\bar{\mathbf{k}}\sigma} (a_{\bar{\mathbf{q}}} + a_{\bar{\mathbf{q}}}^\dagger) + \sum_{\bar{\mathbf{q}}} \omega_{\bar{\mathbf{q}}} a_{\bar{\mathbf{q}}}^\dagger a_{\bar{\mathbf{q}}} \quad (8)$$

where $h_{\bar{\mathbf{k}}}$ describes the band structure in general. The derivation and specific forms of Hamiltonian with hBN and bandwidth are detailed in the Supplementary Information sections X and XI.

It is important to note that the first term in equation (8) does not commute with the second term in this generalized case, making the Lang–Firsov transformation unsuitable for this case. To simulate the polaronic dressing in this generalized Hamiltonian, we employ a variational ansatz of the ground state $|\Psi_G\rangle = U_{\text{NGS}}^\dagger(\lambda) |\Psi_e\rangle |0_{\text{ph}}\rangle$ with

$$U_{\text{NGS}}^\dagger(\lambda) = \exp \left[\frac{\lambda}{\sqrt{N_m}} \sum_{\bar{\mathbf{R}} \sigma \bar{\mathbf{q}} \nu} e^{-i\bar{\mathbf{R}} \cdot \bar{\mathbf{q}}} \mathbf{d}_{\bar{\mathbf{R}}\sigma}^\dagger \eta \mathbf{d}_{\bar{\mathbf{R}}\sigma} (a_{\bar{\mathbf{q}}\nu} - a_{-\bar{\mathbf{q}}\nu}^\dagger) \right] \quad (9)$$

where λ is the variational parameter in contrast to the fixed g/ω_0 of the Lang–Firsov transformation for TBG. Owing to the high phonon energy compared with any energy scales in equation (8), we still assume the post-transformation phonon state is vacuum. Therefore, the variational ansatz gives the total energy as a function of λ :

$$E_{\text{tot}}(\lambda) = \langle 0_{\text{ph}} | \langle \Psi_e | U_{\text{NGS}}^\dagger(\lambda) H U_{\text{NGS}}(\lambda) | \Psi_e \rangle | 0_{\text{ph}} \rangle \\ = E_{\text{kin}} - \frac{N_\nu}{N_m} (2g\lambda - \omega_0 \lambda^2) \sum_{\bar{\mathbf{R}} \bar{\mathbf{R}}' \sigma \sigma' \bar{\mathbf{q}}} e^{i(\bar{\mathbf{R}}' - \bar{\mathbf{R}}) \cdot \bar{\mathbf{q}}} \\ \langle \Psi_e | (\mathbf{d}_{\bar{\mathbf{R}}\sigma}^\dagger \eta \mathbf{d}_{\bar{\mathbf{R}}\sigma}) (\mathbf{d}_{\bar{\mathbf{R}}'\sigma'}^\dagger \eta \mathbf{d}_{\bar{\mathbf{R}}'\sigma'}) | \Psi_e \rangle \quad (10)$$

with the normalized kinetic energy E_{kin} follows the expression in Supplementary Information sections X and XI. Unlike the analytically solvable Lang–Firsov transformation, the variational parameter λ is obtained by numerical optimization of $E_{\text{tot}}(\lambda)$. The self-consistent equations for different situations of the generalized Hamiltonian are derived in Supplementary Information sections X and XI. This numerically determined λ describes the relative strength of the polaronic dressing, where λ reproduces g/ω_0 when H takes the flat-band TBG form in equation (3). The Poisson factor for the relative replica intensity is then obtained by $p = N_\nu \lambda^2$.

Data availability

The data that support the findings of this study are available from the corresponding authors upon reasonable request.

51. Kim, K. et al. Van der Waals heterostructures with high accuracy rotational alignment. *Nano Lett.* **16**, 1989–1995 (2016).

52. Miao, W., Li, C., Han, X., Pan, D. & Dai, X. Truncated atomic plane wave method for the subband structure calculations of moire systems. *Phys. Rev. B* **107**, 125112 (2023).

Acknowledgements We acknowledge discussion with I. Esterlis, D. H. Lee, L. Fu, B. Lian and Y. He. Y.C. acknowledges the support from the Oxford–ShanghaiTech collaboration project and the Shanghai Municipal Science and Technology Major Project (grant 2018SHZDZX02). A.Y. acknowledges support from the Gordon and Betty Moore Foundation’s EPiQS initiative grant GBMF9469, DOE-BES grant DE-FG02-07ER46419, NSF-MRSEC through the Princeton Center for Complex Materials NSF-DMR-2011750, NSF-DMR-1904442, ARO MURI (W911NF-21-2-0147), and ONR N00012-21-1-2592. The quantum phonon model and simulations (S.D., H.Y. and Y.W.) are supported by the US Department of Energy, Office of Science, Basic Energy Sciences, under Early Career Award number DE-SC0024524. B.A.B.’s work was primarily supported by the DOE grant number DE-SC0016239, the Simons Investigator Grant number 404513. Sabbatical support was provided by the European Research Council (ERC) under the European Union’s Horizon 2020 research and innovation programme (grant agreement number 101020833) and by ONR grant number N00014-20-1-2303. C. Liu acknowledges the support through the Penn State MRSEC–Center for Nanoscale Science via NSF award DMR-2011839 and grant NSF PHY-1748958 to the Kavli Institute for Theoretical Physics (KITP). Z.L. acknowledges the support from the National Natural Science Foundation of China (92365204, 12274298) and the National Key R&D program of China (grant number 2022YFA1604400/03). L.H. acknowledges the support from the National Natural Science Foundation of China (grant numbers 12141401, 12425405). This work was supported by a fellowship and a CRF award from the Research Grants Council of the Hong Kong Special Administrative Region, China (projects no. HKUST SRFS2324-6S01 and no. C7037-22GF). ARPES simulations were obtained using the Frontera computing system at the Texas Advanced Computing Center. This research used resources of the Advanced Light Source, a US DOE Office of Science User Facility under contract number DE-AC02-05CH11231.

Author contributions Y.C. conceived of and supervised the ARPES experiments. A.Y. supervised the device fabrication and STM and STS experiments. K.P.N., D.W., M.O., R.L.L., C.H. and L.H. fabricated the devices used for the study. C.C., S.H., C.P., D. Pei, Y.L., H.X., H.G., Q.L. and Z.L. performed the ARPES measurements and data analysis. K.P.N., D.W., M.O. and R.L.L. carried out the STM and STS measurements. S.D., H.Y. and Y.W. developed the strong-coupling electron–phonon theory with help from B.A.B. and C. Liu and conducted spectral simulations. W.M., C. Li, X.H., D. Pan and X.D. simulated the coupling matrix elements. S.Z. and J.L. conducted tight-binding ARPES simulations. C.J., A.B. and E.R. maintained the ARPES beamline. K.W. and T.T. synthesized the hBN crystals. All authors discussed the results and contributed to the writing of the paper.

Competing interests The authors declare no competing interests.

Additional information

Supplementary information The online version contains supplementary material available at <https://doi.org/10.1038/s41586-024-08227-w>.

Correspondence and requests for materials should be addressed to Yao Wang or Yulin Chen. **Peer review information** *Nature* thanks Neil Wilson and the other, anonymous, reviewer(s) for their contribution to the peer review of this work.

Reprints and permissions information is available at <http://www.nature.com/reprints>.